Comparative analysis of different wave turbine designs based on conditions relevant to northern coast of Egypt

Ahmed S. Shehata [a, b, *], Qing Xiao [a], Mohamed El-Shaib [b], Ashraf Sharara [b], Day Alexander [a]

[a] Department of Naval Architecture, Ocean and Marine Engineering, University of Strathclyde, Glasgow, G4 0LZ, UK
[b] Marine Engineering Department, College of Engineering and Technology, Arab Academy for Science Technology and Maritime Transport, P.O. 1029, AbuQir, Alexandria, Egypt

ARTICLE INFO

ABSTRACT

Wave energy has a great potential to solve the unrelenting energy deficiency in Egypt. The present work recommends Wells turbine as a suitable choice for the Egyptian coasts due to its simple and efficient operation under low input air flow. In addition, the possibility of extracting the wave energy from the Egyptian coasts was investigated using the oscillating water system based on real data from the site. To achieve this purpose, two-dimensional numerical models for Wells turbine airfoils, functioning under sinusoidal wave flow conditions, were built. Moreover, the running and starting characteristics under sinusoidal-flow conditions were investigated using a mathematical code. The results were discussed using the first law analysis, in addition to the second law analysis by using the entropy generation minimization method. It was found that the NACA0015 airfoil always gives a global entropy generation rate that is less than other airfoils by approximately −14%, −10.3% and −14.7% for the sinusoidal wave with time periods equal to 4, 6 and 8 s respectively. Moreover, the effects of blade profile, time period and solidity on the output power (kW) value were discussed.

1. Introduction

Egypt is now struggling to meet its own energy needs, experiencing one of its most serious energy crises for decades. The number of residents has increased by a million people over the past six months only, and global warming has caused an increase in the use of air conditioning in summer. Egypt's demand for electricity is growing rapidly and the need to develop alternative power resources is becoming ever more urgent, which necessitates looking for renewable energy options to help meet the increasing demand. For this end, the development of the renewable energy industry has become a priority over the recent years for the Egyptian government. The utilization of wave energy systems has escalated significantly over the past two decades, generally depending on oscillating water column (OWC) concept [1–3]. Wells turbine is one of the most efficient OWC technologies [4]. The characteristic feature of Wells turbine is that oscillating air flow produces a single direction rotation of the rotor without the use of a rectifying valve [5–9]. Wells turbine is usually characterized by four digit double zero NACA profile [10–13], where the shape of the NACA four digit profiles is determined by three parameters: the camber (first digit), the position of the camber (second digit), and the percentage of thickness to chord (third and fourth digits). Hence, profiles without a camber are symmetrical (NACA 00XX).

The overall performance of several design types of Wells turbine were investigated in Ref. [14] by using a semi-empirical method for predicting the turbine's performance in Ref. [15]. Similar comparisons were undertaken using an experimental measurement in Ref. [16]. It was observed that the contra-rotating turbine had an operational range which was similar to that of the monoplane turbine with guide vanes, and achieved similar peak efficiency. However, the resulting flow from the contra-rotating turbine was better than the monoplane turbine with guide vanes in the post-stall regime.

In order to improve the performance of the Wells turbine, the effect of end plate on the turbine characteristics was investigated in Refs. [17,18]. Using an experimental model and CFD method, it was shown that the peak efficiency increased by 4% approximately,

* Corresponding author. Department of Naval Architecture, Ocean and Marine Engineering, University of Strathclyde, Glasgow, G4 0LZ, UK.
E-mail address: ahmed.mohamed-ahmed-shehata@strath.ac.uk (A.S. Shehata).

Nomenclature

A	The total blade area. A = (z c b), m^2
A_r	Rotor area $= \pi R_m^2$, m^2
a	Margin distance for the end plate, m
b	Blade Span, m
c	Blade chord, m
C_D	Drag force coefficient
C_L	Lift force coefficient
C_P	Power coefficient
C_T	Torque coefficient
D	Drag Force, N
D_r	Rotor diameter, m
f	Wave frequency, Hz
F_A	Axial Force, N
F_t	Tangential Force, N
g	Leading edge offsetting of a blade from an axis, m
I	Moment of inertia, kg m^2
L	lift Force, N
Δp	Pressure difference across the turbine, N/m^2
Q	Flow rate through the rotor area, m^3/sec
R_h	Rotor radius at hub, m
R_m	Mean rotor radius $= \frac{R_t + R_h}{2}$, m
R_r	Rotor radius, m
R_t	Rotor radius at tip, m
Q	Flow rate through the rotor area, m^3/sec
S_{gen}	Local entropy generation rate (W/m^2K)
S_G	Global entropy generation rate (W/K)
S_{ij}	Mean strain rate
S_t	Thermal entropy generation rate (W/m^2K)
S_V	Viscous entropy generation rate (W/m^2K)
T_o	Reservoir temperature (K)
t_{sin}	The time period for sinusoidal wave $= 1/f$, sec
T_L	Loading torque N m
TSR	Tip speed ratio $= \frac{\omega Rm}{V_{Am}}$
$\bar{u}_i$	Reynolds Averaged velocity component in i direction (m/s)
V	Axial velocity $= V_A \sin\left(\frac{2\pi t}{T}\right)$, m/s
V_A	Maximum value of axial velocity, m/s
V_r	Resultant air velocity, m/s
V_o	Initial velocity for computation (m/s)
W^*	Output power coefficient
W_{rev}	Reversible work
X_i	Inertia coefficient
X_L	Loading torque coefficient
Z	Number of blades
α	Angle of attack- the angle between the chord line and the direction of the fluid velocity, degree
η	Mean turbine efficiency
ρ	Air specific density, kg/m^3
σ	Turbine solidity $= \frac{Z\,C}{2\,\pi\,R_m}$
ϕ	Flow coefficient
ω	Rotor angular velocity, rad/sec

compared to the Wells turbine without an end plate. The calculations of the blade sweeps for the Wells turbine were investigated using a numerical code by Ref. [19] and experimentally with quasi-steady analysis in Ref. [20]. As a result, it was found that the performance of the Wells turbines was influenced by the blade sweep area. To achieve a high performance for the turbine, the appropriate sweep ratio selected was found to be 35%. In addition, setting the blades at their optimum pitch angle during compression and suction was expected to substantially improve turbine efficiency [8,21–28]. This setting for the blades is achieved by the turbine manufacturer in such a way that allows the turbine blades to rotate around their axis with an angle equals to ± optimum blade setting pitch angle. Furthermore, two-stage Wells turbines with symmetric and non-symmetric airfoils were investigated in Ref. [29]; the numerical algorithms were used to estimate the optimum shape of the airfoil with an increase of efficiency (by 2.1%) and of tangential force coefficient (by 6%), compared to the standard NACA 2421.

Exergy analysis was performed using the numerical simulation for steady state biplane Wells turbines in Ref. [30], where the upstream rotor had a design point second law efficiency of 82.3%, although the downstream rotor second law efficiency was equal to 60.7%. The entropy generation, due to viscous dissipation, around different 2D airfoil sections for Wells turbine was recently investigated by the authors in Refs. [31,32]. When Reynolds number increased from 6 × 104 to 1 × 105, the total entropy generation increased correspondingly by more than two folds for both airfoils. However, when Reynolds number further increased further to 2 × 105, the total entropy generation exhibited unintuitive values ranging from 25% less to 20% higher than the corresponding value at Reynolds number = 1 × 105. The efficiency of four different airfoils in compression cycle was found to be higher than suction cycle at a two-degree angle of attack. But when the angle of attack increased, the efficiency of suction cycle increased more than the

compression one. This study suggested that there is a possible existence of a critical Reynolds number at which viscous irreversibilities take minimum values. Moreover, a comparison of total entropy generation, due to viscous dissipation, between a suggested design (variable chord) and a constant chord Wells turbine was presented in Ref. [33]. The detailed results demonstrated an increase in static pressure difference around new blade and a 26.02% average decrease in total entropy generation throughout the full operating range.

Most of the researchers investigated the performance of different airfoils designs and different operational conditions where analyzing the problem was based only on the parameter of first law of thermodynamics. It is essential to look at the second law of thermodynamics to form a deeper understanding of the problem, since it has shown very promising results in many applications, such as wind turbine in Refs. [34–39] and gas turbine in Refs. [40–44]. A numerical optimization algorithm based on CFD simulation was implemented in order to optimize the blade pitch angle in Refs. [45,46]. The standard NACA0021 and an optimized profile (AOP) were numerically investigated. The present CFD optimization results showed that the optimum blade pitch angle for NACA0021 was +0.3° while that of the AOP was equal to +0.6°. The present airfoils with the optimized pitch angle showed an average efficiency with an improvement of 3.4% for standard NACA0021 and 4.3% for the AOP.

The most bustling with life coast of the Southern Mediterranean Basin is the Egyptian coast, lying between the Nile Delta and the Libyan borders, with a potential of above 3.35 kW/m wave power in summer and 6.8 kW/m in winter [47,48], and wave energy of about 36003 kWh/m. The most active sea states have significant wave heights ranging between 1 and 4 m, and wave energy periods between 4 and 8 s. The regions with increased wave energy potential are mainly the western and southern coastlines of Cyprus Island,
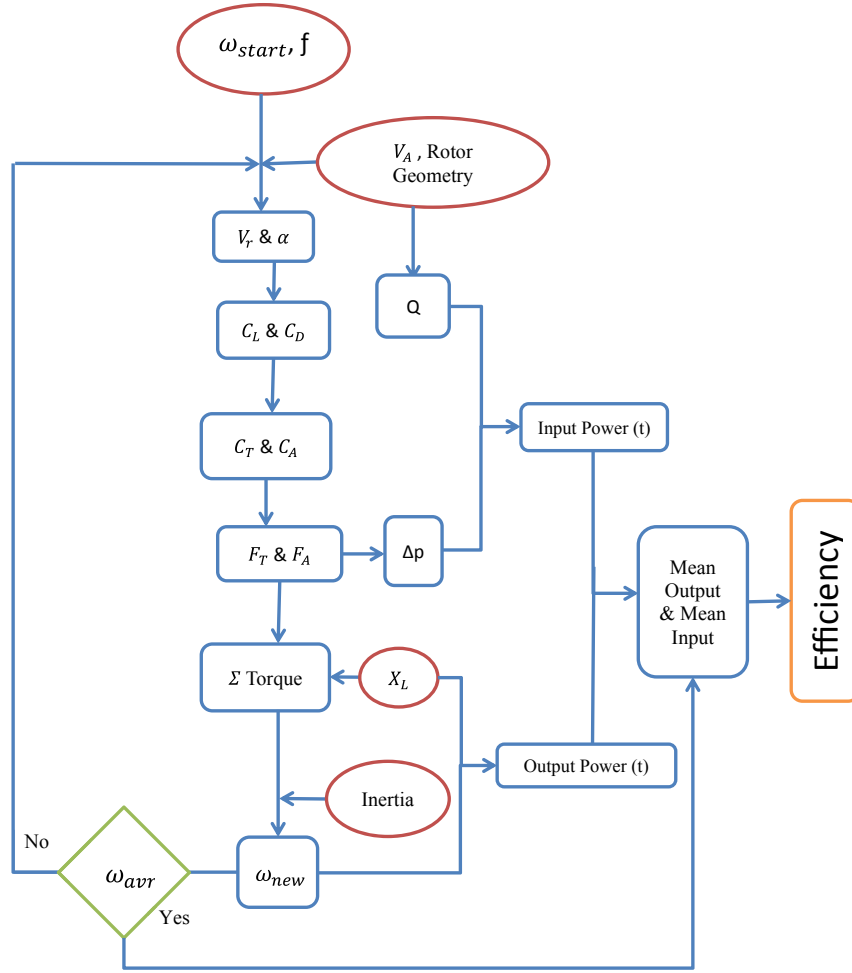
Fig. 1. Flow chart of implementing analytical mathematical model on Wells turbine performance.

the sea area of Lebanon and Israel, as well as the coastline of Egypt, especially around Alexandria. The significant differences between the sea in Egypt and other seas are that the sea wave in Egypt is relatively low but also stable. Hence, the potential wave energy can be revealed and exploited [49]. Otherwise, sea states with wave heights greater than 5 m are not very important for the annual energy [50].

The objective of this work is to carry out a study to prove that the Wells turbine could be a suitable wave energy extractor for the Egyptian coasts and breakwater, through a study on the force analysis (torque coefficient) and velocity analysis (global entropy generation rate) for different turbine airfoils. To achieve this goal, the CFD technique was used along with an analytical model that investigated the main flow characteristics and estimated the hydrodynamics output power. According to the literature, it is the first time to study the availability of extracted wave energy around Egyptian coast area via a Wells turbine.

2. Mathematical formulations

This section describes the first law analysis method used in this study to measure. In addition, the efficiency calculations for the Wells turbine under sinusoidal-flow conditions were studied using an analytical mathematical model. The net torque which drives the Wells turbine is resultant of the summation of all torques exerted on the turbine as follows:

$$\sum Torque = T_{aerodynamic} - T_{Load} - T_{Loss} \qquad (1)$$

$$\sum Torque = \frac{1}{2}\rho\left(V_a^2 + (\omega\,R_m)^2\right)A\,R_mC_T - T_L - T_{Loss} \qquad (2)$$

where T_L is the load torque.

By applying the angular moment equation of motion along turbine axis, we get

$$I\frac{d\omega}{dt} = \sum Torque \qquad (3)$$

where I is the rotor mass moment of inertia and ω is the angular velocity of the rotor varying with time.

Neglecting the torque losses and substituting from eq. (2) into (3) we get:

$$I\frac{d\omega}{dt} = \frac{1}{2}\rho\left(V_a^2 + (\omega\,R_m)^2\right)z\,c\,b\,R_mC_T - T_L \qquad (4)$$

The load torque can be expressed in a non-dimensional form as:

$$X_L = \frac{T_L}{\rho\pi R_m^3 V_a^2} \qquad (5)$$

Hence, the rotor equation of motion is:

$$I\frac{d\omega}{dt} = \frac{1}{2}\rho\left(V_a^2 + (\omega R_m)^2\right) z\, c\, b\, R_m C_T - X_L \rho \pi R_m^3 V_a^2 \tag{6}$$

$$\frac{d\omega}{dt} = \frac{\frac{1}{2}\rho\left(V_a^2 + (\omega R_m)^2\right) z\, c\, b\, R_m C_T - X_L \rho \pi R_m^3 V_a^2}{I} \tag{7}$$

$$\int d\omega = \int \frac{\frac{1}{2}\rho\left(V_a^2 + (\omega R_m)^2\right) z\, c\, b\, R_m C_T - X_L \rho \pi R_m^3 V_a^2}{I}\, dt \tag{8}$$

$$\omega_2 - \omega_1 = \frac{\frac{1}{2}\rho\left(V_a^2 + (\omega R_m)^2\right) z\, c\, b\, R_m C_T - X_L \rho \pi R_m^3 V_a^2}{I}\, t_2 - t_1 \tag{9}$$

For the first law of thermodynamics, the lift and drag coefficient C_L and C_D are computed from the post processing software. Then, the torque coefficient can be expressed as [51]:

$$C_T = (C_L \sin\alpha - C_D \cos\alpha) \tag{10}$$

The flow coefficient ϕ relating tangential and axial velocities of the rotor is defined as:

$$\phi = \frac{V_a}{\omega * R_m} \tag{11}$$

where the α angle of attack is equal to:

$$\alpha = \tan^{-1}\frac{V_a}{\omega R_m} \tag{12}$$

The mean output power is expressed as:

$$Output\ Power = T_L * \omega_{avr} \tag{13}$$

where ω_{avr} is the average velocity during a complete cycle given by:

$$\omega_{avr} = \frac{1}{T}\int_0^T \omega(t)dt \tag{14}$$

Hence, the output is

$$Output\ Power = X_L * \pi * \rho * V_{Am}^2 * R_m^3 * \omega_{avr} \tag{15}$$

where X_L is the non-dimensional loading torque.

$$Input\ power = \frac{1}{T}\int_0^T \Delta P * Q dt \tag{16}$$

where Q is the volume flow rate passing through the rotor area to the turbine and given by:

$$Q = V_A A_r \tag{17}$$

The efficiency in the first law of thermodynamics (μ_F) is defined as:

$$\mu_F = mean\ value\ of\ \frac{Output\ Power}{Input\ Power} = \frac{\frac{1}{T}\int_0^T T_L\omega(t)\, dt}{\frac{1}{T}\int_0^T \Delta P * Q\, dt} \tag{18}$$

Fig. 1 shows the flow chart that displays the main steps that apply the mathematical model using the MATLAB software. These steps are based on the equations that are derived above, starting from setting the initial angular velocity which causes the initial motion, and operational conditions. The aim is to calculate the generated force on the blade, the instantaneous angular velocity, the output power, and the turbine efficiency. In this work, the rotor geometry data from existing Wells turbine projects (the OSPREY) [52] is used as inlet parameters for the mathematical model. This is in addition to the operating condition data based on the real data from the site, namely, the Southern Mediterranean Basin [50].

3. Numerical methodology

The numerical simulations were conducted with the commercial CFD software ANSYS Fluent. The unsteady Navier-Stokes equations were solved by a finite volume for an incompressible flow and turbulence was modeled using the Large Eddy Simulation. The governing equations employed for Large Eddy Simulation (LES) were obtained by filtering the time-dependent Navier-Stokes equations. The filtering process was chosen as it effectively filters out eddies whose scales are smaller than the filter width or grid spacing used in the computations. The resulting equations, thus, govern the dynamics of large eddies. A filtered variable (denoted by an over-bar) is defined by:

$$\overline{\phi}(x) = \int_D \phi(x')G(x,x')dx' \tag{19}$$

where D is the fluid domain and G is the filter function that determines the scale of the resolved eddies. In FLUENT, the finite-volume discretization itself implicitly provides the filtering operation [53]:

$$\overline{\phi}(x) = \frac{1}{V}\int_V \phi(x')dx',\ x' \in V \tag{20}$$

where V is the volume of a computational cell, the filter function, G (x, x'), implied here is then

$$G(x,\ x') = \begin{cases} 1/V\ for\ x' \in V \\ 0\ otherwise \end{cases} \tag{21}$$

The LES model was applied to essentially incompressible (but not necessarily constant-density) flows. Filtering the incompressible Navier-Stokes equations, one obtained [54]

$$\frac{\partial\rho}{\partial t} + \frac{\partial\rho\overline{u}_i}{\partial x_i} = 0 \tag{22}$$

$$\frac{\partial}{\partial t}(\rho\overline{u}_i) + \frac{\partial}{\partial x_j}(\rho\overline{u}_i\overline{u}_j) = \frac{\partial}{\partial x_j}\left(\mu\frac{\partial\overline{u}_i}{\partial x_j}\right) - \frac{\partial\overline{p}}{\partial x_i} - \frac{\partial\tau_{ij}}{\partial x_j} \tag{23}$$

where τ_{ij} is the sub-grid-scale stress defined by

$$\tau_{ij} = \rho\overline{u_i u_j} - \rho\overline{u}_i\ \overline{u}_j \tag{24}$$

The sub-grid-scale stresses resulting from the filtering operation were unknown, and required modeling. The majority of sub-grid-scale models were eddy viscosity models of the following form:

$$\tau_{ij} - \frac{1}{3}\tau_{kk}\sigma_{ij} = -2\mu_t\overline{S}_{ij} \tag{25}$$

where $\overline{S}_{ij}$ is the rate-of-strain tensor for the resolved scale defined by:
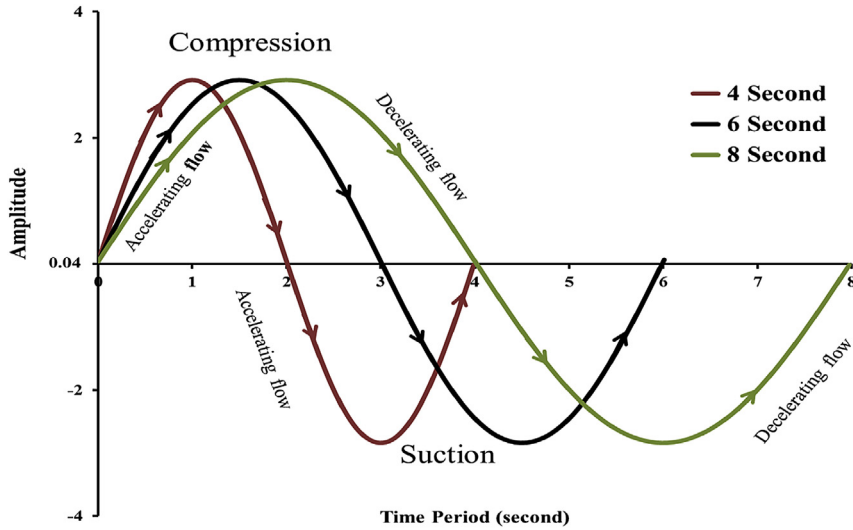
Fig. 2. The sinusoidal waves boundary condition, which represents a regular oscillating water column.

Table 1
Specification of grids.

Grid	No. of cells	First cell	Growth rate	Aspect ratio	Equi-angle skew
A	112603	1×10^{-4}	1.02	1.996	0.429
B	200017	1×10^{-5}	1.015	2.466	0.475
C	312951	1×10^{-5}	1.012	2.376	0.514
D	446889	1×10^{-6}	1.01	2.551	0.513

$$\overline{S}_{ij} = \frac{1}{2}\left(\frac{\partial \overline{u}_i}{\partial x_j} + \frac{\partial \overline{u}_j}{\partial x_i}\right) \qquad (26)$$

and μ_t is the sub-grid-scale turbulent viscosity, for which the Smagorinsky-Lilly model is used. The most basic of sub-grid-scale models for "Smagorinsky-Lilly model" was proposed by Smagor-
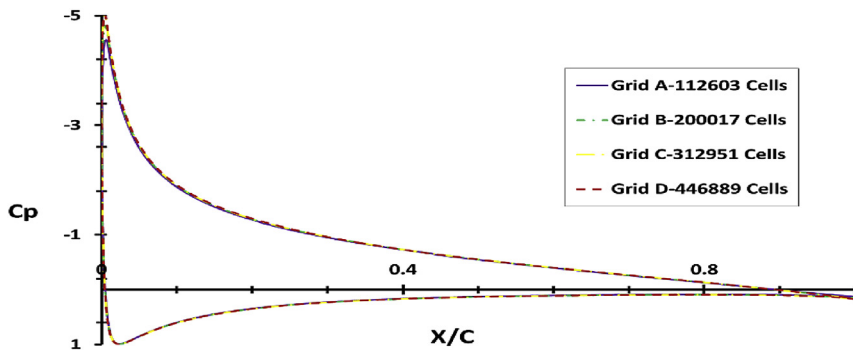

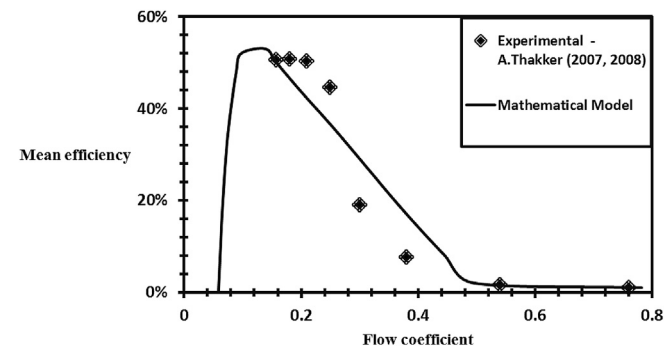**Fig. 3.** Pressure coefficient plotted on the normalized airfoil cord at different grid resolutions.

insky [55] and further developed by Lilly [56]. In the Smagorinsky-Lilly model, the eddy viscosity is modeled by:

$$\mu_t = \rho L_s^2 \, |\overline{S}| \qquad (27)$$

where L_s is the mixing length for sub-grid-scale models and $|\overline{S}| = \sqrt{2\overline{S}_{ij}\overline{S}_{ij}}$. The L_s is computed using:

$$L_s = \min\left(kd, \, C_s V^{1/3}\right) \qquad (28)$$

where C_s is the Smagorinsky constant, $k = 0.42$, d is the distance to the closest wall, and V is the volume of the computational cell. Lilly derived a value of 0.23 for C_s from homogeneous isotropic turbulence. However, this value was found to cause excessive damping of large-scale fluctuations in the presence of mean shear or in transitional flows. $C_s = 0.1$ was found to yield the best results for a wide range of flows.
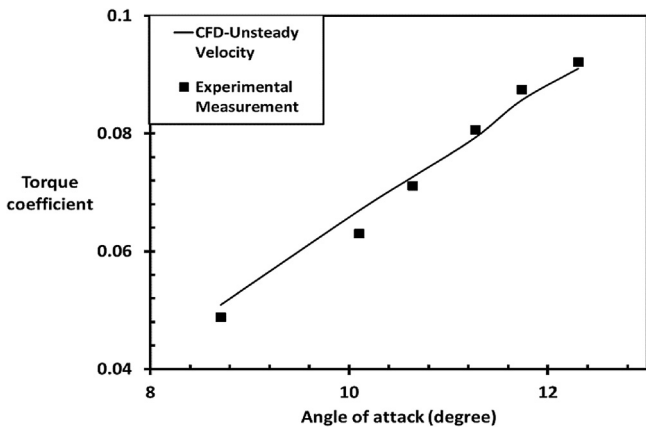

Fig. 4. Mean efficiency of NACA0015 under sinusoidal flow conditions with solidity = 0.64.

Fig. 5. Measured torque coefficient from reference (63–65) and calculated torque coefficient from CFD unsteady flow with sinusoidal inlet velocity.

The transport equations of such models can be found in turbulence modeling texts such as [57]. The second law of thermodynamics defines the net-work transfer rate as [58]:

$$\dot{W}_{rev} - \dot{W} = T_o S_{gen} \tag{29}$$

With the use of entropy analysis method, it is possible to express the irreversible entropy generation in terms of the derivatives of local flow quantities in the absence of phase changes and chemical reactions. The two dissipative mechanisms in viscous flow are the strain-originated dissipation and the thermal dissipation, which correspond to a viscous and a thermal entropy generation respectively [59], and can be expressed as:

$$S_{gen} = S_V + S_{th} \tag{30}$$

In incompressible isothermal flow, such as the case in hand, the thermal dissipation term vanishes. The local viscous irreversibilities, therefore, can be expressed as:
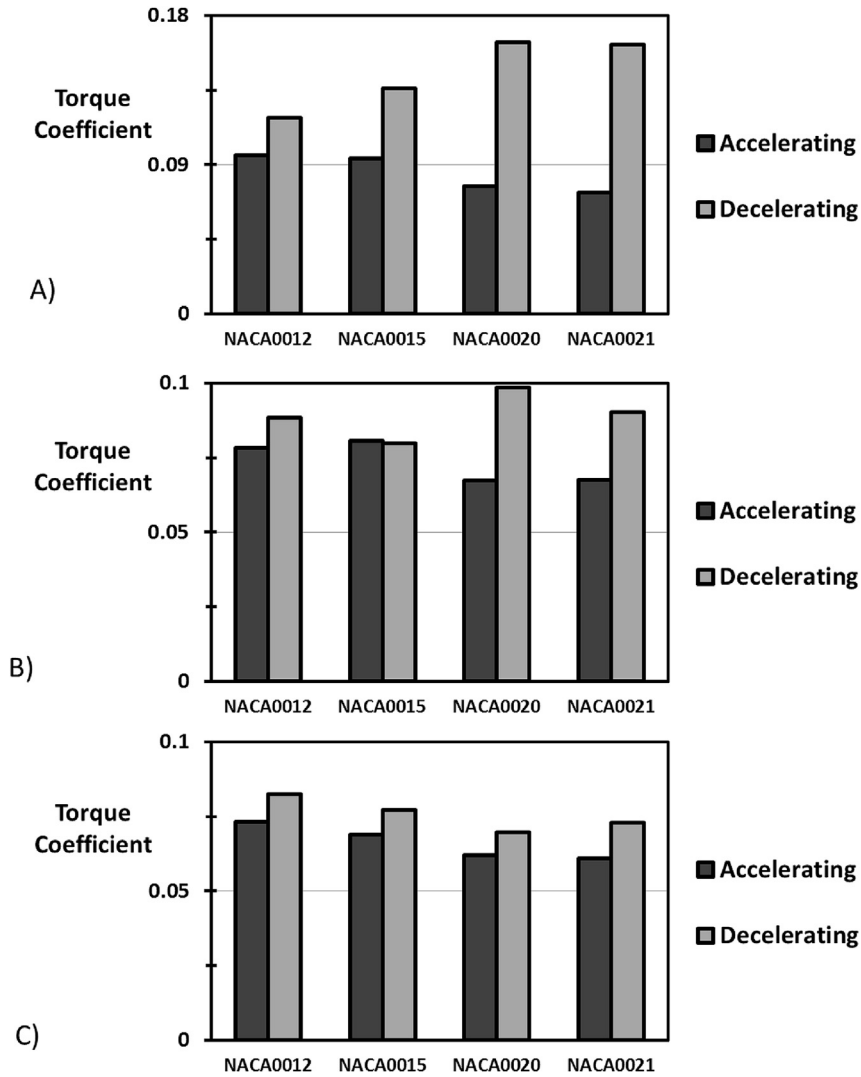

Fig. 6. Comparisons between the torque coefficient during the accelerating and decelerating flow for four different airfoils, A) $t_{sin} = 4$ s, B) $t_{sin} = 6$ s and C) $t_{sin} = 8$ s.
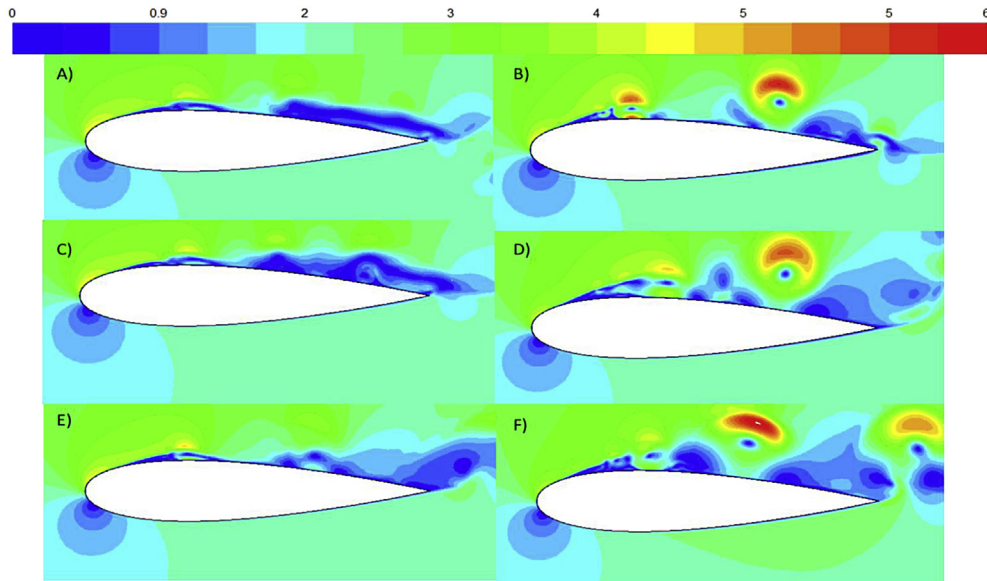
Table 2
The percentage of torque coefficient difference between decelerating and accelerating flow.

| Airfoil section	C_T at decelerating flow is higher than that in accelerating flow by		
	For t_{sin} equal to 4 s	For t_{sin} equal to 6 s	For t_{sin} equal to 8 s
NACA0012	24%	13%	12.5%
NACA0015	45%	−1%	12%
NACA0020	114%	46%	13%
NACA0021	122%	33%	20%

$$S_V = \frac{\mu}{T_o}\dot{\phi} \tag{31}$$

where $\dot{\phi}$ is the viscous dissipation term that is expressed in two dimensional Cartesian coordinates as [59]:

$$\dot{\phi} = 2\left[\left(\frac{\partial u}{\partial x}\right)^2 + \left(\frac{\partial v}{\partial y}\right)^2\right] + \left(\frac{\partial u}{\partial y} + \frac{\partial v}{\partial x}\right)^2 \tag{32}$$

Fig. 7. Contour of velocity magnitude at velocity equal to 2.08 (m/s) around the NACA0020 airfoil for sinusoidal input flow, Accelerating flow A) $t_{sin} = 4$ s, C) $t_{sin} = 6$ s, E) $t_{sin} = 8$ s and Decelerating flow B) $t_{sin} = 4$ s, D) $t_{sin} = 6$ s, F) $t_{sin} = 8$ s.
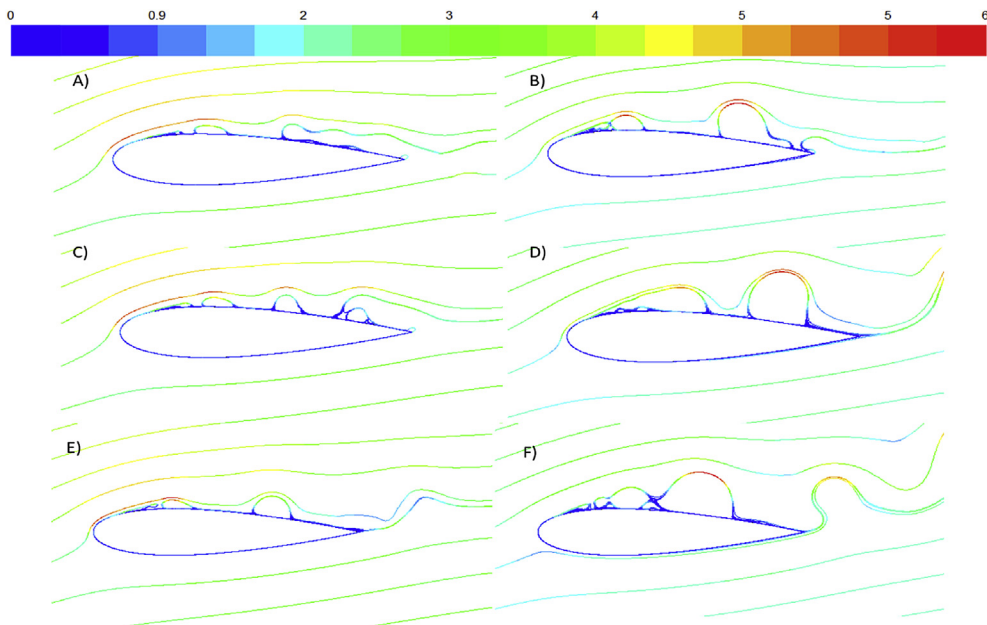
Fig. 8. Path line of velocity magnitude at velocity equal to 2.08 (m/s) around the NACA0020 airfoil for sinusoidal input flow, Accelerating flow A) $t_{sin} = 4$ s, C) $t_{sin} = 6$ s, E) $t_{sin} = 8$ s and Decelerating flow B) $t_{sin} = 4$ s, D) $t_{sin} = 6$ s, F) $t_{sin} = 8$ s.
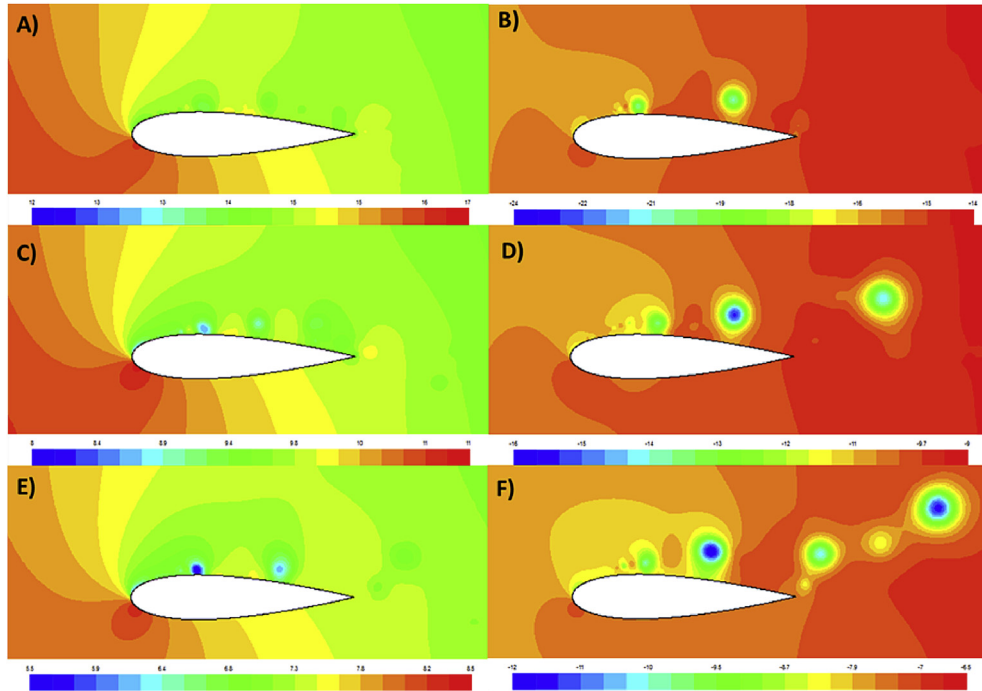
Fig. 9. Contours of pressure coefficient around the airfoil, Accelerating flow A) $t_{sin} = 4$ s, C) $t_{sin} = 6$ s, E) $t_{sin} = 8$ s and Decelerating flow B) $t_{sin} = 4$ s, D) $t_{sin} = 6$ s, F) $t_{sin} = 8$ s.

and the global entropy generation rate is hence expressed as [31]:

$$S_G = \iint_{xy} S_V \, dy \, dx \tag{33}$$

and finally, the second law efficiency is defined as [32]:

$$\eta_S = \frac{KE}{Exergy} \tag{34}$$

where $Exergy = KE + S_G$ and $KE = \frac{1}{2}V^2$.

From the above equation, it can be concluded that the increase in torque coefficient leads to an increase in the first law efficiency. On the other hand, the decrease in the global entropy generation rate leads to an increase in the second law efficiency.

3.1. Computational model and boundary conditions

Two-dimensional numerical models for NACA0015 airfoils were built up and validated against experimental measurements under unsteady flow conditions. The computational domain was discretized to Cartesian structured finite volume cells using GAMBIT code. The second order upwind interpolation scheme was used in this work, where its results were approximately similar to those yielded by third order MUSCL scheme in the present situation. In addition, in some cases the third order MUSCL scheme showed high oscillatory residual during the solution.

The axial flow of Wells Turbine is modeled as a sinusoidal wave in this simulation. Therefore, inlet boundary conditions are set to change with time. In order to apply the inlet boundary condition, inlet velocity with periodic function (see Fig. 2) is generated as follows:

$$V_{(t)} = V_o + V_A \sin(\sin 2\pi f t_{sin}) \tag{35}$$

where t_{sin} is equal to (4, 6, and 8) seconds and is set as one period in this simulation, considering the real data from the Egyptian coasts.

The time step is set as 0.000296721 s in order to satisfy CFL (Courant Friedrichs Lewy) condition equal to 1 [60]. Furthermore, the sinusoidal wave condition creates various Reynolds numbers up to 2×10^4.

### 3.2. Grid sensitivity test (verification)

In order to ensure that the numerical model is free from numerical diffusion and artificial viscosity errors, several grid numbers were tested to estimate the number of grid cells required to establish a grid-independent solution. Table 1 shows the specifications of different grids used in unsteady two-dimensional models with constant velocity. Fig. 3 shows the pressure coefficient distribution on the upper and lower surfaces of the NACA0012 airfoil as computed by the four grids. Grid D required more time than grid C, yielding similar results. Therefore, grid C was chosen to conduct the analysis presented hereafter.

4. Models validation

4.1. Validation of the analytical model

The experimental data from Refs. [61,62] for an unsteady flow was used to validate our analytical mathematical model. The experimental data from a test rig was used by Wave Energy Research Team, University of Limerick. It consisted of a bell mouth entry, test section, drive and transmission section, a plenum chamber with honeycomb section, a calibrated nozzle, and a centrifugal fan. The turbine test section had an internal diameter of 600 mm and a fabricated rotor of a 598 mm diameter, leaving a tip clearance of 1 mm. The hub diameter is 358.8 mm, providing a hub to tip ratio of 0.6 and chord length of 120 mm. The turbine was mounted on a shaft in a cylindrical annular duct. The shaft was coupled to motor/generator via a torque meter. The turbine blades (8 blades for solidity = 0.64 and 6 blades for solidity = 0.48) were set on the hub at a 90° angle of stagger along the y-axis. Fig. 4 shows
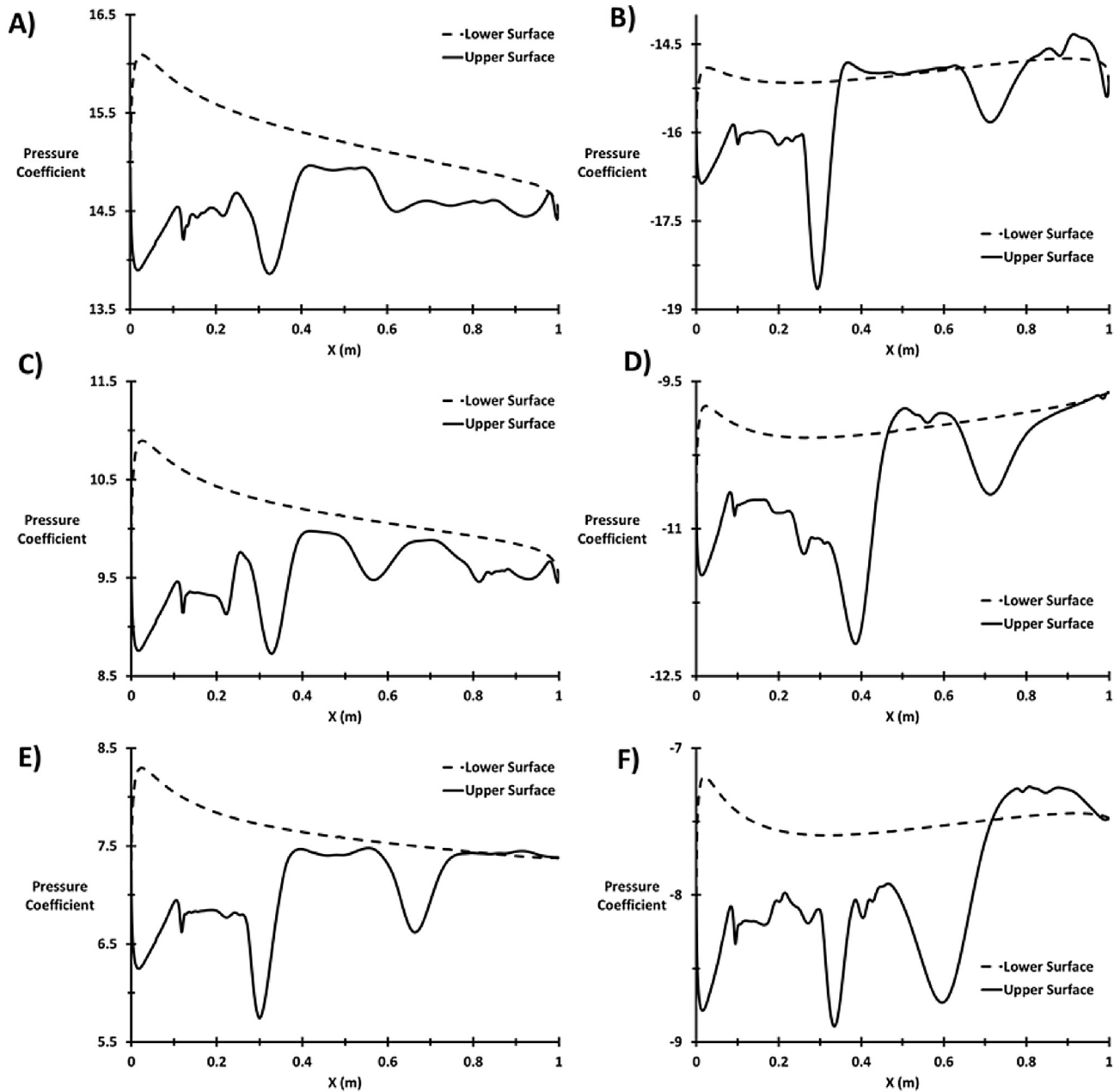
Fig. 10. Pressure coefficient distribution on the upper and lower surface of the airfoil, Accelerating flow A) t_{sin} = 4 s, C) t_{sin} = 6 s, E) t_{sin} = 8 s and Decelerating flow B) t_{sin} = 4 s, D) t_{sin} = 6 s, F) t_{sin} = 8 s.

a good agreement between the mean efficiency from Refs. [61,62] with t_{sin} equal to 9.2 s, and the predicted mean efficiency from the mathematical code at same t_{sin}.

4.2. Validation of the CFD model

Large Eddy Simulation model was used to model the flow around NACA0015 airfoil in order to give the best agreement with experimental data adopted from Refs. [63–65]. The Eddy model proved effective, where the data was used to simulate and validate the CFD model as it had a suitable Reynolds number equal to 2×10^4, and where the torque coefficient result was clear. The validation case details for Wells turbine prototype are characterized by the following parameters: hub radius, is equal to 101 mm; tip radius, equal to 155 mm; NACA0015 blade profile with constant

chord length, equal to 74 mm; and a number of blades, equal to 7. Therefore, the hub-to-tip ratio and the solidity are equal to 0.65 and 0.64, respectively. The blades were produced with composite material reinforced by carbon fiber with suitable attachment. The experimental data was at steady flow conditions. Therefore, the average value for the lift and drag coefficient was used to calculate one value for the torque coefficient for each angle of attack. Fig. 5 displays the result of using the computational model under sinusoidal inlet flow velocity with experimental data from Refs. [63–65]. A very good agreement was achieved.

5. Results and discussion

The CFD models were used, the results of which simulated the compression cycle with accelerating and decelerating flow.
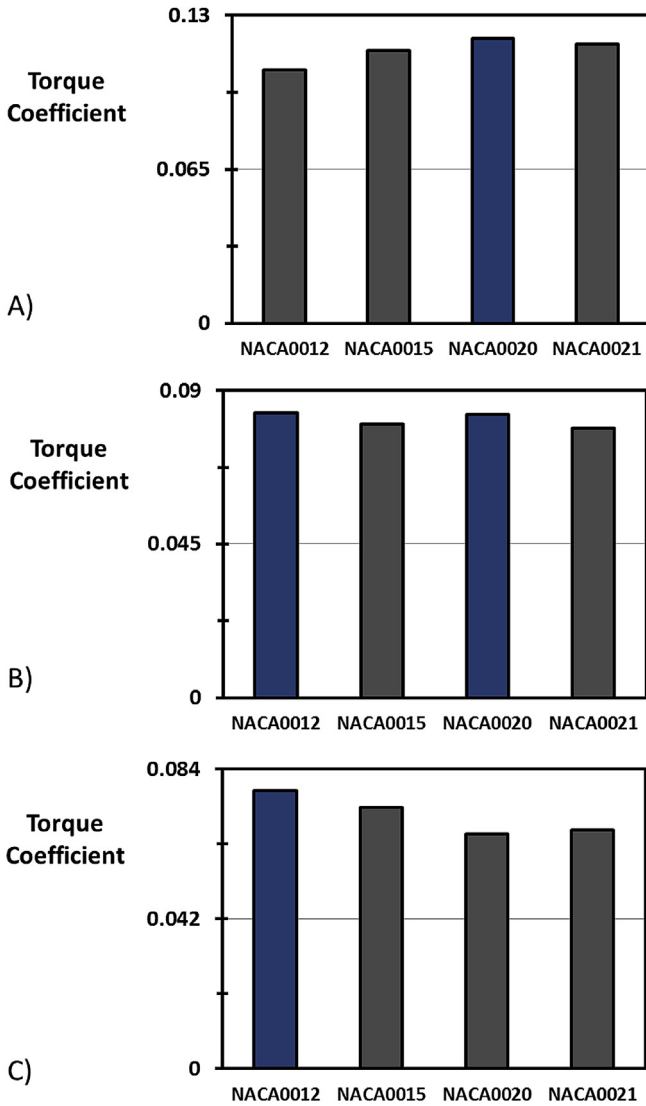
Fig. 11. Total average values for the torque coefficient during the velocity cycle for the four different airfoils, A) t_{sin} = 4 s, B) t_{sin} = 6 s and D) t_{sin} = 8 s.

Otherwise, the wave cycle with the compression and suction stage was used in the analytical method.

5.1. First law of thermodynamics analysis

The comparison between the torque coefficient for accelerating and decelerating flow with four different airfoils was shown in Fig. 6. It can be noted that the sinusoidal wave with t_{sin} of 4 s has a large torque coefficient. Moreover, the torque coefficient value at decelerating flow is always higher than that at accelerating flow, except NACA0015 for sinusoidal wave with 6 s. In addition, the sinusoidal wave with 8 s has the smallest difference in torque coefficient values between accelerating and decelerating flow as show in Table 2.

To understand the reasons why the torque coefficient at decelerating flow is mostly higher than that at accelerating flow, the contours and path line of velocity around the blade were investigated. Figs. 7 and 8 show the contours and path line of velocity magnitude around the NACA0020 airfoil blade at the same instantaneous velocity (2.08 m/s). It can be shown that at an accelerating flow, the airfoil has very low velocities (see Fig. 7) and
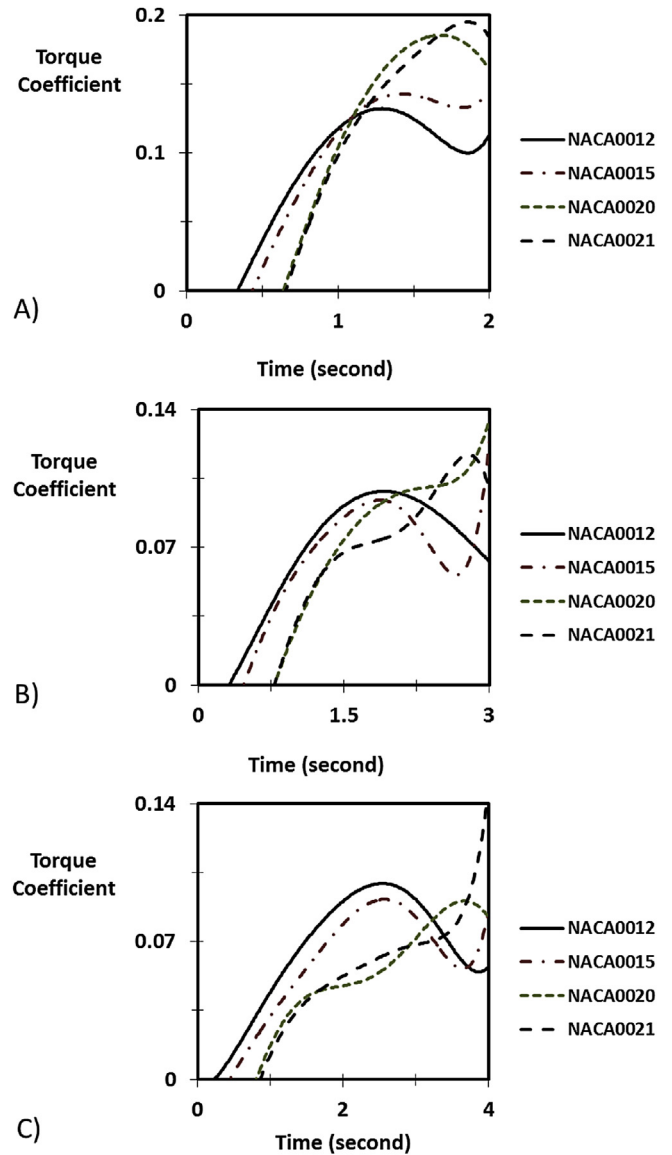

Fig. 12. The instantaneous values for the torque coefficient during the compression cycle for four different airfoils, A) t_{sin} = 4 s, B) t_{sin} = 6 s and D) t_{sin} = 8 s.
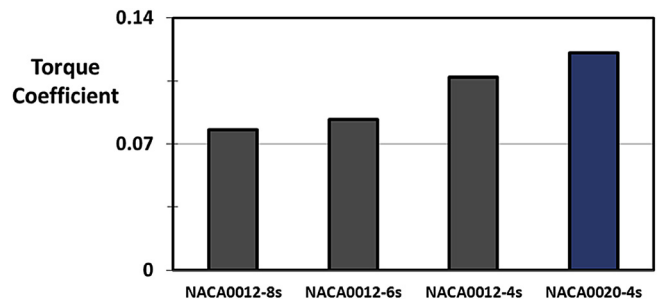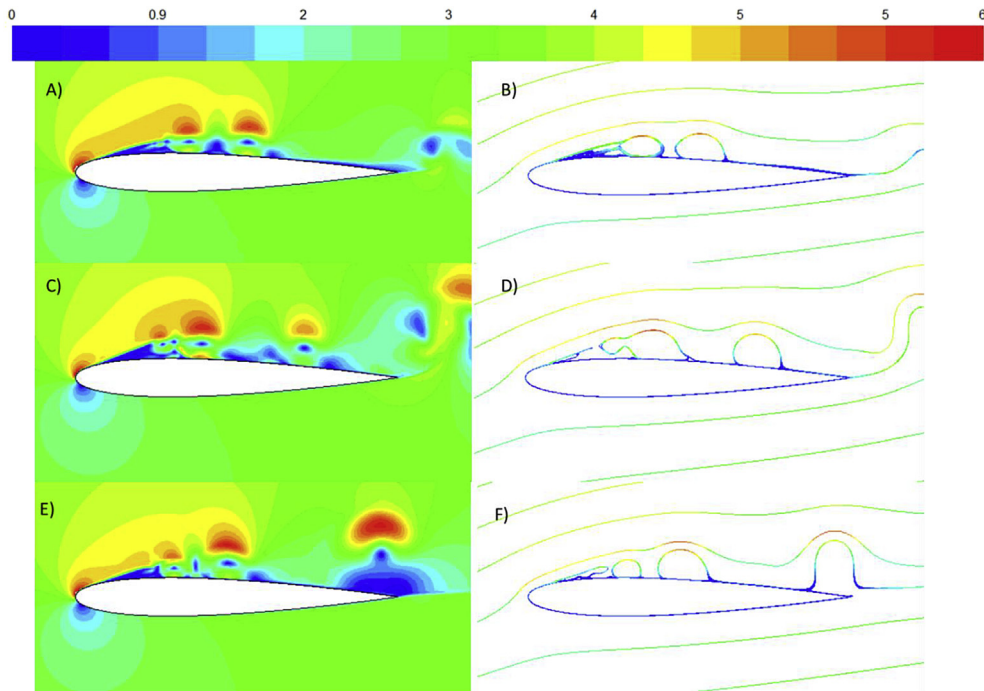

Fig. 13. The comparison between the maximum torque coefficients for each velocity cycle.

a high separation layer (see Fig. 8) at the trailing edge area than that in a decelerating flow condition. This difference between the accelerating and the decelerating flow decreases, with an increase in t_{sin} for the sinusoidal wave.

Fig. 14. Contours of velocity magnitude at maximum velocity equal to 2.92 (m/s) around the NACA0012 airfoil for sinusoidal input flow, A) $t_{sin} = 4$ s, C) $t_{sin} = 6$ s, E) $t_{sin} = 8$ s, and path line colored by velocity magnitude for B) $t_{sin} = 4$ s, D) $t_{sin} = 6$ s, F) $t_{sin} = 8$ s.(For interpretation of the references to colour in this figure legend, the reader is referred to the web version of this article.)

Figs. 9 and 10 show the pressure distribution around the upper and lower surface of NACA0020, at accelerating and decelerating flow, and at velocity equal to 2.09 m/s with different time periods. The difference between the pressure value at upper and lower surface has a direct effect on the torque coefficient value, whereby, this difference at decelerating flow was lower than that at accelerating flow except t_{sin} with 8 s. This behaviour is the same as that of the torque coefficient value. When comparing between the accelerating and decelerating flow, it can be noted that the decelerating flow has a negative pressure value. Furthermore, the increase in time period is accompanied by a decrease in pressure value at accelerating flow. On the other hand, the increase in time period is accompanied by an increase in pressure value at decelerating flow. The low-pressure area was shown around the trailing edge, and increased with the increase of time period.

The total average torque coefficient during the cycle for four different airfoils at different time periods was shown in Fig. 11. It can be concluded that the sinusoidal wave, with t_{sin} equal to 4 s, has the highest torque coefficient, where, NACA0020 (with t_{sin} equal to 4 s) gives a torque coefficient higher than NACA0012 by 13%, NACA0015 by 5% and NACA0021 by 2%. For the sinusoidal wave with t_{sin} of 6 s, the airfoil NACA0012 gives a torque coefficient higher than NACA0015 by 4%, but it was approximately the same as NACA0020, with an increase of only 0.6%. Also, NACA0012 gives a torque coefficient that is 6% higher than NACA0021. Finally, for the sinusoidal wave with t_{sin} equal to 8 s, the NACA0012 gives a torque coefficient higher than NACA0015 by 7%, NACA0020 by 18% and NACA0021 by 17%.

Fig. 12 shows the instantaneous torque coefficient at a compression cycle for different airfoils (NACA0012, NACA0015, NACA0020 and NACA0021) with different time periods (4 s, 6 s and 8 s). It can be seen that in the first half of each cycle (accelerating flow), NACA0012 always has a higher torque coefficient. The comparison between the maximum torque coefficient values for each time period cycle was shown in Fig. 13. The NACA0012 airfoil

section has the highest value at sinusoidal wave cycles with t_{sin} equal to 6 s and with t_{sin} equal to 8 s. On the other hand, the NACA0020 airfoil section has the highest value at the sinusoidal wave cycle with t_{sin} equal to 4 s. In addition, the NACA0020 airfoil section (with t_{sin} equal to 4 s) creates a torque coefficient more than NACA0012 (with t_{sin} equal to 8 s) by 54%, NACA0012 (with t_{sin} equal to 6 s) by 44%, and NACA0012 (with t_{sin} equal to 4 s) by 13%.

Fig. 14 highlights the effect of the low velocity area and separation layer at trailing edge by velocity contours and path line around the NACA0012 airfoil at a maximum velocity of 2.92 m/s. It is clear that the torque coefficient is influenced by the low velocity area and separation layer at trailing edge. When the low velocity area at trailing edge increases, the torque coefficient value decreases. Similarly, as the separation layer at trailing edge increases, the torque coefficient value also decreases. The pressure distribution around the upper and lower surface of airfoil at accelerating and decelerating flow was shown in Fig. 15 at a maximum velocity of (2.92 m/s), with different time periods (4, 6 and 8 s). The higher disturbances occurring in separation layers at the upper surface than those occurring at the lower surface (Fig. 14) is due to the irregular values of pressure at the upper surface. The low pressure areas around the trailing edge increase the separation layer at the trailing edge; therefore, the separation layers at a 4 s time period have lowest disturbances and lowest low-pressure areas around the trailing edge. Table 3 summarizes the torque coefficient at different time periods (t_{sin} equal to 4 s, 6 s and 8 s) for the four airfoils (NACA0012, NACA0015, NACA0020 and NACA0021).

5.2. Second law of thermodynamics analysis

Fig. 16 highlights the comparison between the global entropy generation rate for accelerating and decelerating flows for the four different airfoils. All airfoils in the accelerating flow create global entropy generation rate lower than that created in the decelerating flow. The difference in the global entropy generation rate between
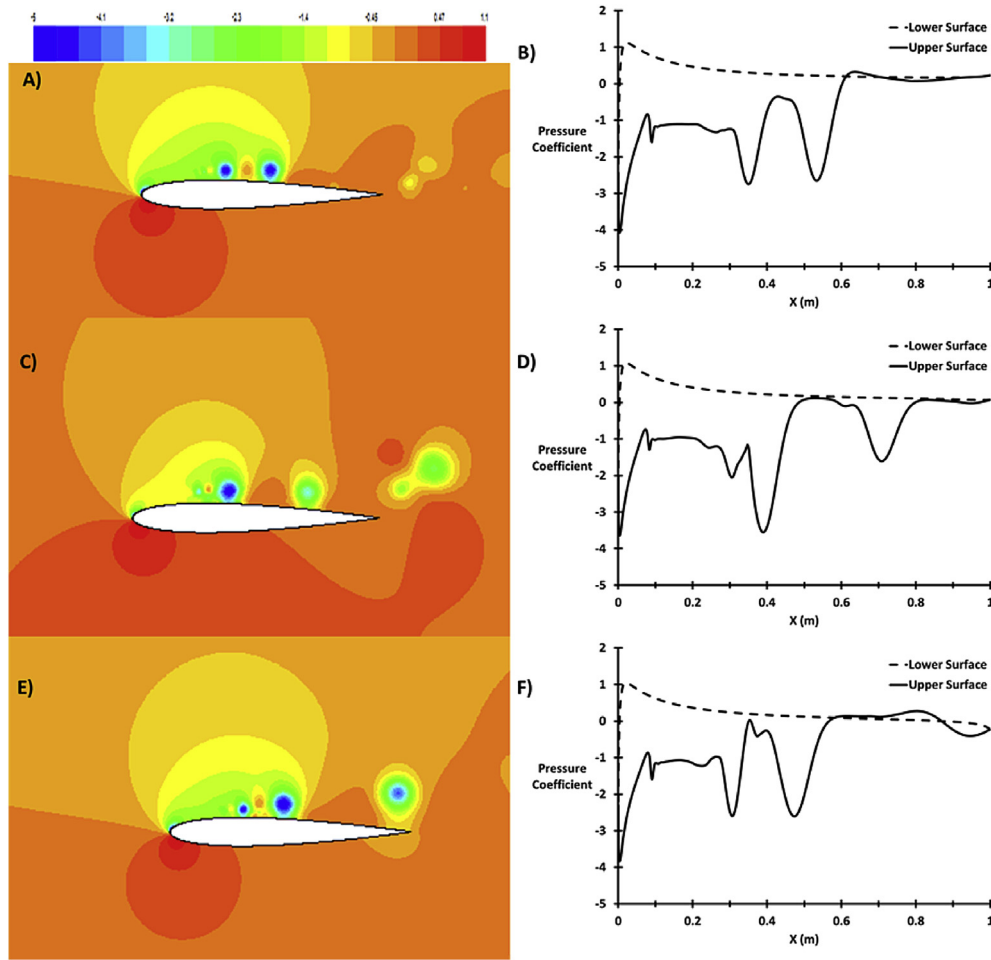
Fig. 15. Contours of pressure coefficient A) $t_{sin} = 4$ s, C) $t_{sin} = 6$ s, E) $t_{sin} = 8$ s, and Pressure coefficient distribution on the upper and lower surface of the airfoil B) $t_{sin} = 4$ s, D) $t_{sin} = 6$ s, F) $t_{sin} = 8$ s.

Table 3
A summary of the torque coefficient values at different time periods for the four airfoils.

Airfoil section	C_T ($t_{sin} = 4$ s)			C_T ($t_{sin} = 6$ s)			C_T ($t_{sin} = 8$ s)		
	Accelerating	Decelerating	Average	Accelerating	Decelerating	Average	Accelerating	Decelerating	Average
NACA0012	0.096	0.118	0.107	0.078	0.0885	0.0834	0.073	0.0825	0.0779
NACA0015	0.094	0.136	0.115	0.08	0.08	0.080	0.069	0.0773	0.0731
NACA0020	0.077	0.164	0.12036	0.0675	0.099	0.0829	0.0619	0.06984	0.0659
NACA0021	0.07	0.163	0.11799	0.0676	0.0902	0.0789	0.0608	0.0729	0.0669

the accelerating and decelerating flows is not influenced by the change in time period (see Table 4). As an average for all airfoils, the sinusoidal wave cycle with t_{sin} of 8 s has the lowest difference in S_G between accelerating and decelerating flows for the four different airfoils.

The contours of global entropy generation rate around the NACA0021 at the instantaneous velocity (2.08 m/s) for the accelerating and decelerating flow were represented in Fig. 17. It can be seen that the global entropy generation rate around the airfoil section in the decelerating flow was higher than that in the accelerating flow at the three different time periods (as noted above in Fig. 16). The average value of the global entropy generation rate for each airfoil during the sinusoidal cycle with three different time periods was shown in Fig. 18. It can be concluded that the NACA0015 has the lowest value of the global entropy generation rate at the three different time periods (4 s, 6 s and 8 s), when it was

compared with other airfoils (NACA0012, NACA0020 and NACA0021). See Table 5 for more details.

Fig. 19 shows the contours of the global entropy generation rate at a maximum velocity (2.92 m/s) around NACA0015 airfoil with three different time periods. It can be seen that NACA0015 at sinusoidal wave with t_{sin} equal to 8 s has a lower global entropy generation rate than other time periods for the same airfoil (NACA0015) and same velocity (2.92 m/s). Hence, Fig. 20 compares between the values of S_G (Fig. 20, A) and μ_S (Fig. 20, B) for NACA0015 at three different time periods. It can be concluded that the NACA0015 (with t_{sin} equal to 8 s) has lower S_G than NACA0015 (with t_{sin} equal to 6 s) by -6% and NACA0015 (with t_{sin} equal to 4 s) by -3%. In addition, the μ_S of NACA0015 (with t_{sin} equal to 8 s) is higher than NACA0015 (with t_{sin} equal to 6 s) by 1% and NACA0015 (with t_{sin} equal to 4 s) by 2%. Table 6 summarizes the global entropy generation rate values at different time periods (t_{sin} equal to 4 s, 6 s
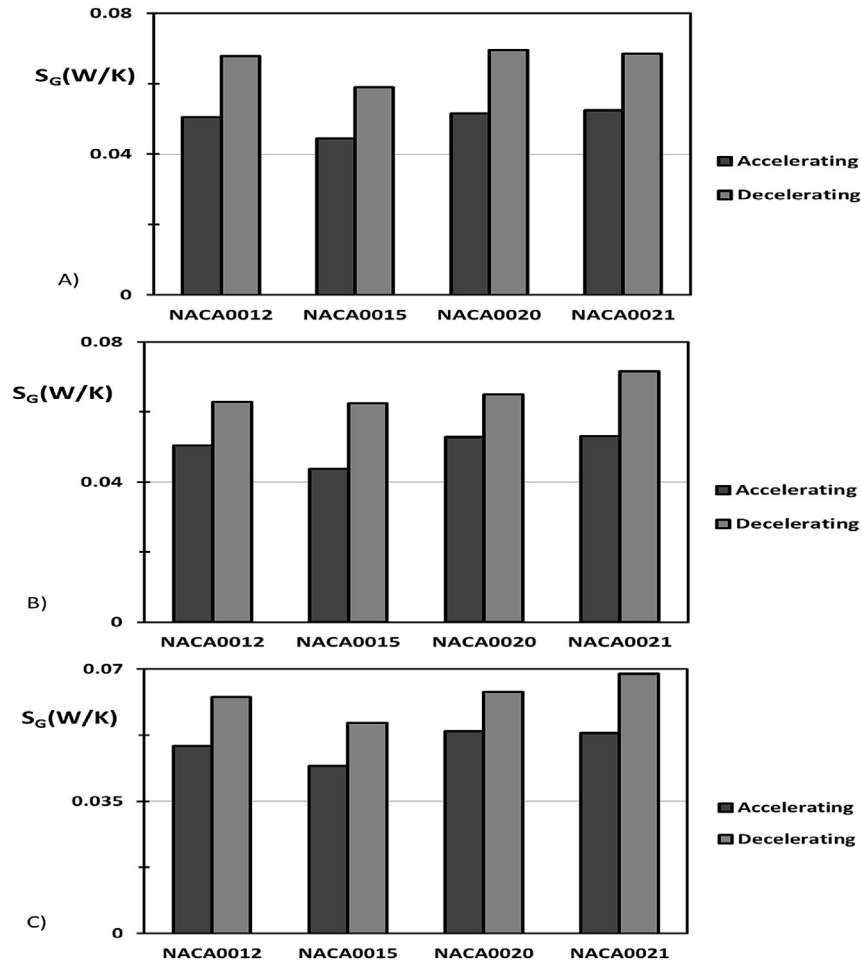
Fig. 16. Comparisons between the global entropy generation rate during the accelerating and decelerating flow for the four different airfoils, A) $t_{sin} = 4$ s, B) $t_{sin} = 6$ s and C) $t_{sin} = 8$ s.

Table 4
The percentage of global entropy generation rate (difference between decelerating and accelerating flow).

Airfoil section	S_G at decelerating flow is higher than that in accelerating flow by		
	For t_{sin} equal to 4 s	For t_{sin} equal to 6 s	For t_{sin} equal to 8 s
NACA0012	34%	25%	26%
NACA0015	33%	43%	26%
NACA0020	35%	23%	19%
NACA0021	31%	35%	30%
Average value	33.3%	31.5%	25.3%

and 8 s) for the four airfoils (NACA0012, NACA0015, NACA0020 and NACA0021).

5.3. Analytical analysis

To examine the effect of wave time period (operating parameter), as well as solidity and airfoil section (design parameters) on the starting and running characteristics, a mathematical analysis was used. It is also used to estimate the turbine efficiency and the output power. The mathematical model gives the relationship of rotor angular velocity with time as a curve in Fig. 21, where the figure shows the NACA0012 airfoil at a time period equal to 6 s with solidity equal to 0.64 in free running condition and with different loading torque coefficients. Furthermore, it can be noted that the

rotor angular velocity was oscillating around a certain average value due to the oscillating inlet velocity.

Fig. 22 represents starting and running characteristics by change in specific parameters, such as time period, solidity and airfoil section. It can be noted that the crawling condition appears at the starting period for the sinusoidal wave cycle with t_{sin} equal to 4 s (Fig. 22A). Otherwise, the three different time periods give the same average velocity (51.6 rad/s) after the starting period. According to Fig. 22B the change in solidity from 0.64 to 0.8 does not have an effect (approximately) on the starting and running characteristics. On the other hand, the NACA0015 airfoil section has the same starting characteristics of NACA0012 but lower rotor average velocity (45.9 rad/s) than NACA0012, see Fig. 22C.

The mean turbine efficiency under sinusoidal flow conditions with different operating and design parameters was shown in Fig. 23. It can be noted that the peak efficiency of the turbine which has sinusoidal wave with t_{sin} equal to 4 s is higher than that with 6 s and 8 s by 8%, as shown in Fig. 23A. It can also be noted that the turbine which has sinusoidal wave with t_{sin} equal to 4 s works with a higher flow coefficient than that with 6 s and 8 s by 17%. Fig. 23B shows that the increase in turbine solidity from 0.64 to 0.8 decreases the peak efficiency by 1% and does not have an effect on the flow coefficient. On the other hand, the change in the airfoil section of a turbine from NACA0012 to NACA0015 does not have an effect on the peak efficiency. However, the turbine with NACA0015 airfoil section works with a higher flow coefficient by 15% than that with NACA0012 airfoil section.
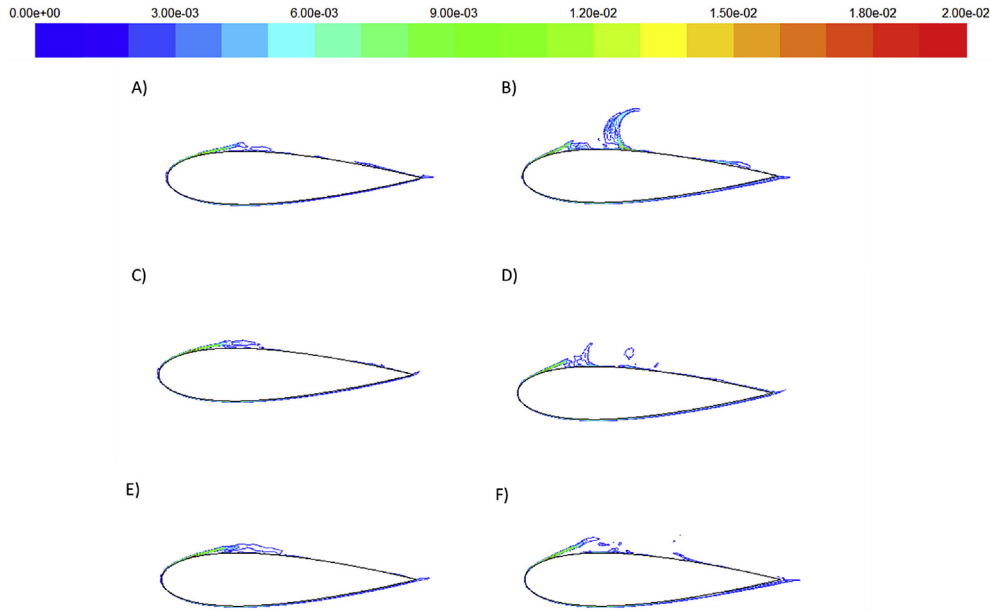
Fig. 17. Contour of global entropy generation rate at velocity equal to 2.08 (m/s) around the NACA0021 airfoil for sinusoidal input flow, A) accelerating flow with t_{sin} = 4 s, B) decelerating flow with t_{sin} = 4 s, C) accelerating flow with t_{sin} = 6 s, D) decelerating flow with t_{sin} = 6 s, E) accelerating flow with t_{sin} = 8 s, F) decelerating flow with t_{sin} = 8 s.
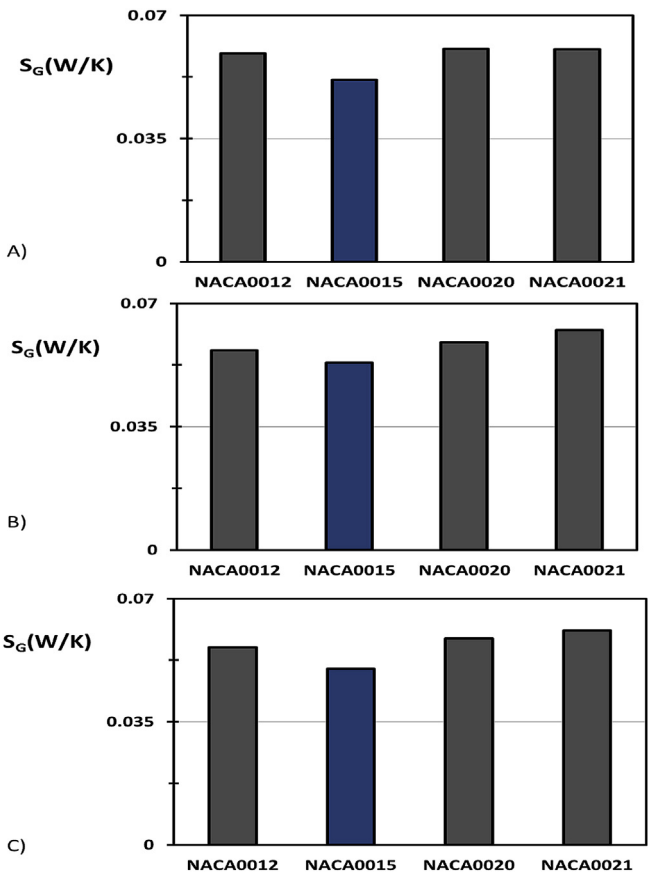

Fig. 18. Total average values for the global entropy generation rate during the velocity cycle for four different airfoils, A) t_{sin} = 4 s, B) t_{sin} = 6 s and D) t_{sin} = 8 s.

Fig. 24 presents the net output power for the Wells turbine under different operating and design parameters based on the real data from the Egyptian northern coast. It can be concluded that the

Table 5
Comparison between S_G for the NACA0015 and other airfoils.

Airfoil section	NACA0015 less than		
	NACA0012	NACA0020	NACA0021
t_{sin} equal to 4 s	−13%	−15%	−14%
t_{sin} equal to 6 s	−6%	−10%	−15%
t_{sin} equal to 8 s	−11%	−15%	−18%

operating condition inlet flow with 6 s time period gives a maximum output power that is higher than 4 s by 19%, and 8 s by 1%, see Fig. 24A. In addition, the change in the design parameters had an effect on the output power value. So, the increase in solidity from 0.64 to 0.8 came with an increase in the net output power by 18% (Fig. 24B). Moreover, Fig. 24C shows that the Wells turbine with NACA0012 airfoil section has a higher net output power than that with NACA0015 airfoil section by 31%. These values were generated from one turbine without any attached guide vans or other enhanced performances, but in the real station, the number of turbine reached two turbines such as the Prototype OWC device (biplane) [66] and LIMPET [67–72] (contra-rotating) in Scotland. Furthermore, the number of turbines can reach four as in the OSPREY [52] used in Scotland or sixteen turbines such as in Mutriku Wave Energy Plant [73,74] in Spain. In addition, the guide vans can be attached to increase the turbine performance such as Mighty Whale [75] in Japan and The Pico Power Plant [76–81] in Portugal.

6. Conclusion

The performance of Wells turbine was investigated by the aerodynamic force (i.e. first law) efficiency as well as the entropy (i.e. second law) efficiency under oscillating flow conditions. The work was performed by using time-dependent CFD models of different NACA airfoils under sinusoidal flow boundary conditions. Besides, an analytical analysis was used to study the starting and running characteristics under sinusoidal flow conditions with different operating and design parameters. Furthermore, the turbine efficiency curve and the net output power were estimated.
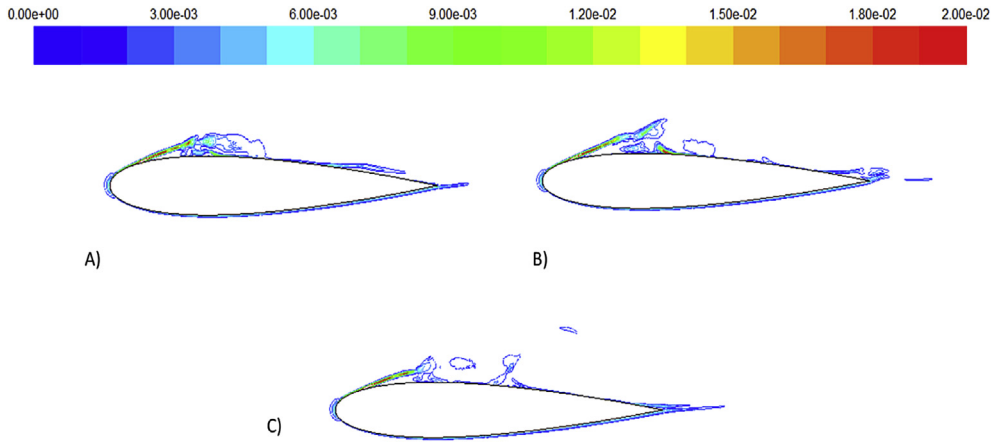
Fig. 19. Contour of global entropy generation rate at maximum velocity equal to 2.92 (m/s) around the NACA0015 airfoil for sinusoidal input flow, A) t_{sin} = 4 s, Bt_{sin} = 6 s and D) t_{sin} = 8 s.
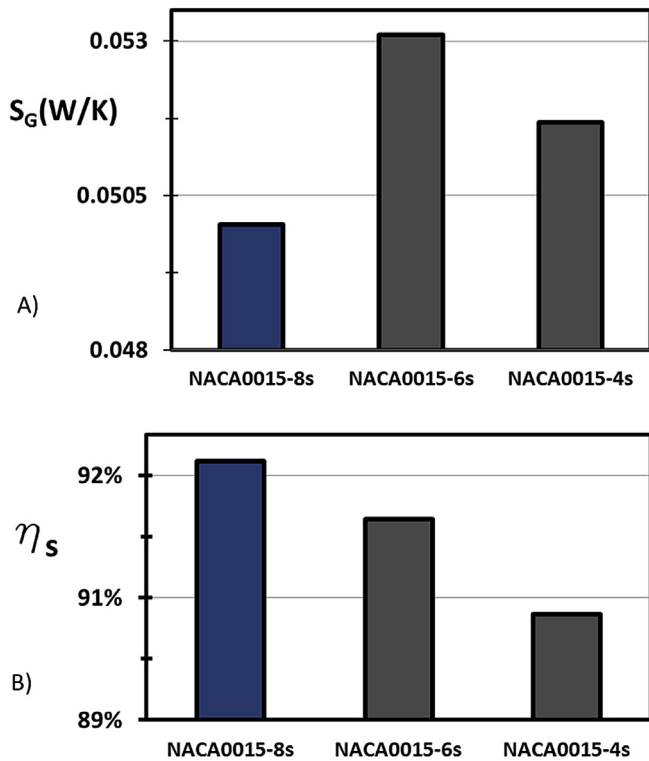

Fig. 20. The comparison between the NACA0015 at three different time periods (8 s, 6 s and 4 s), A) the global entropy generation rate and B) the second law efficiency.
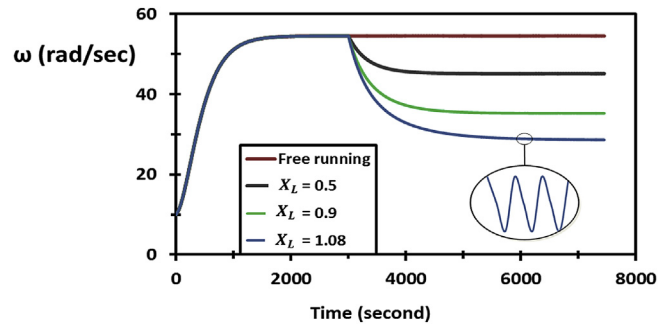

Fig. 21. Angular velocity variations with time for different loading torque coefficient.

t_{sin} equal to 4 s) was higher than NACA0012 (with t_{sin} equal to 8 s) by 54%, NACA0012 (with t_{sin} equal to 6 s) by 44% and NACA0012 (with t_{sin} equal to 4 s) by 13%. Moreover, NACA0015 had shown a decrease in the value of S_G at the three different t_{sin} (4 s, 6 s and 8 s) by −14%, −10.3% and −14.7%, respectively as an average value. On the other hand, for NACA0015, the lowest S_G was generated when t_{sin} was equal to 8 s with an average of −4.5% less S_G than that of t_{sin} equal to 4 and 6 . 2.2 kW was the maximum output power value that can be achieved by Wells turbine with NACA0012 airfoil section and solidity equal to 0.8, under sinusoidal wave with t_{sin} equal to 6 s.

Future research should focus on design optimization to create an optimum design, which has a maximum torque coefficient, a minimum entropy generation, in addition to the highest output

Table 6
A summary of the global entropy generation rate values at different time periods for the four airfoils.

Airfoil section	S_G (kW) t_{sin} = 4 s			S_G (kW) t_{sin} = 6 s			S_G (kW) t_{sin} = 8 s		
	Accelerating	Decelerating	Average	Accelerating	Decelerating	Average	Accelerating	Decelerating	Average
NACA0012	0.0505	0.06785	0.05918	0.05	0.063	0.0567	0.0496	0.06265	0.0561
NACA0015	0.0444	0.05899	0.0517	0.0437	0.0625	0.0531	0.04434	0.0557	0.05003
NACA0020	0.05152	0.06958	0.0606	0.053	0.065	0.0589	0.0535	0.0639	0.0587
NACA0021	0.05239	0.06844	0.0604	0.053	0.072	0.062	0.05302	0.0687	0.06086

From the comparison between the maximum torque coefficient values for each time period cycle it can be concluded that the generating torque coefficient on the NACA0020 airfoil section (with

power value. Furthermore, the study recommends the use of wave energy in Egypt as a way to cut down on excessive high fossil fuel usage.
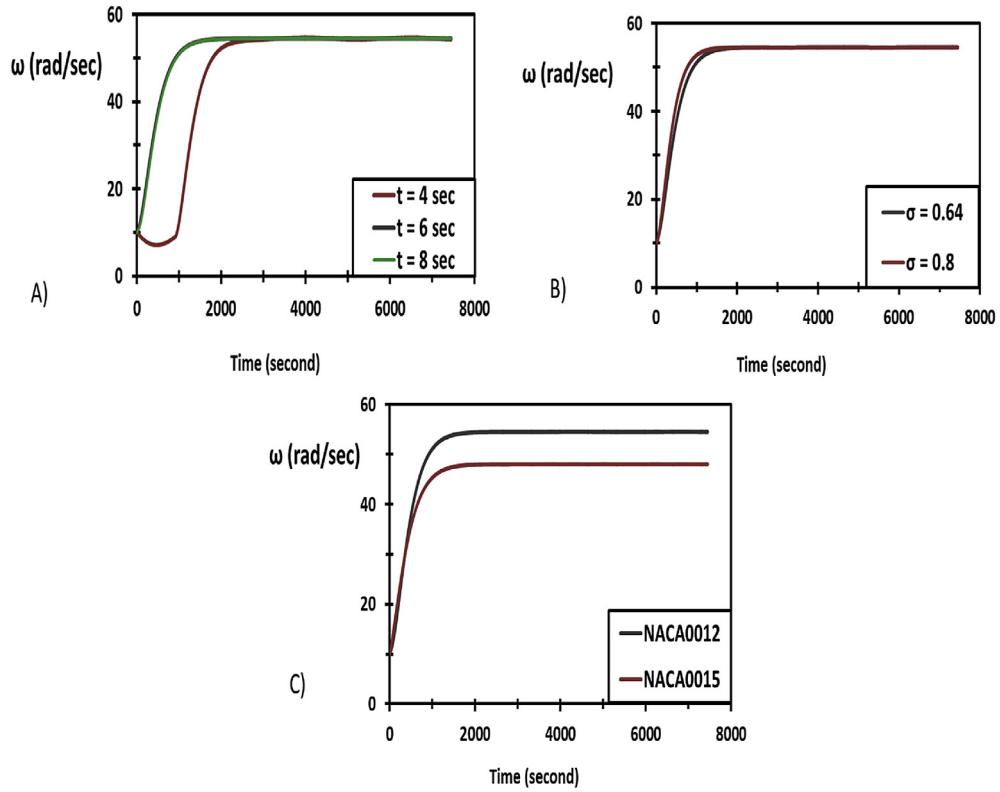
Fig. 22. Angular velocity variation with time in free running condition, A) different time period (t_{sin} = 4 s, 6 s and 8 s), B) different solidity (0.64 and 0.8) and C) different airfoils section (NACA0012 and NACA0015).
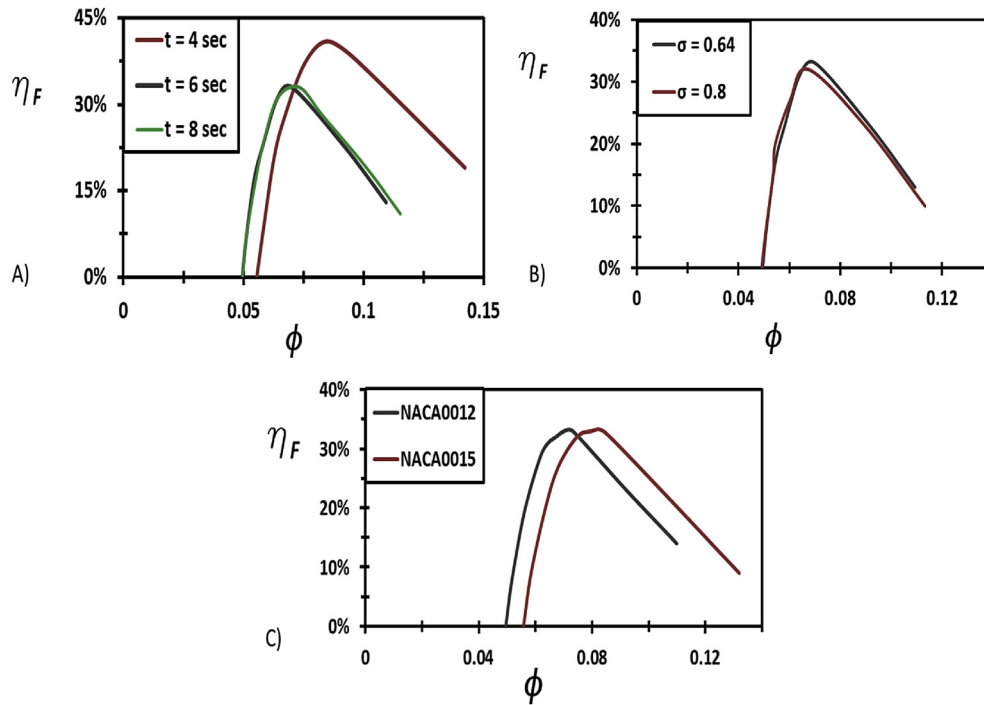
Fig. 23. The mean efficiency of turbine under sinusoidal flow conditions, A) different time periods (t_{sin} = 4 s, 6 s and 8 s), B) different solidity (0.64 and 0.8) and C) different airfoils section (NACA0012 and NACA0015).

Fig. 24. The value of output power for the turbine under sinusoidal flow conditions, A) different time periods (t_{sin} = 4 s, 6 s and 8 s), B) different solidity (0.64 and 0.8) and C) different airfoils section (NACA0012 and NACA0015).
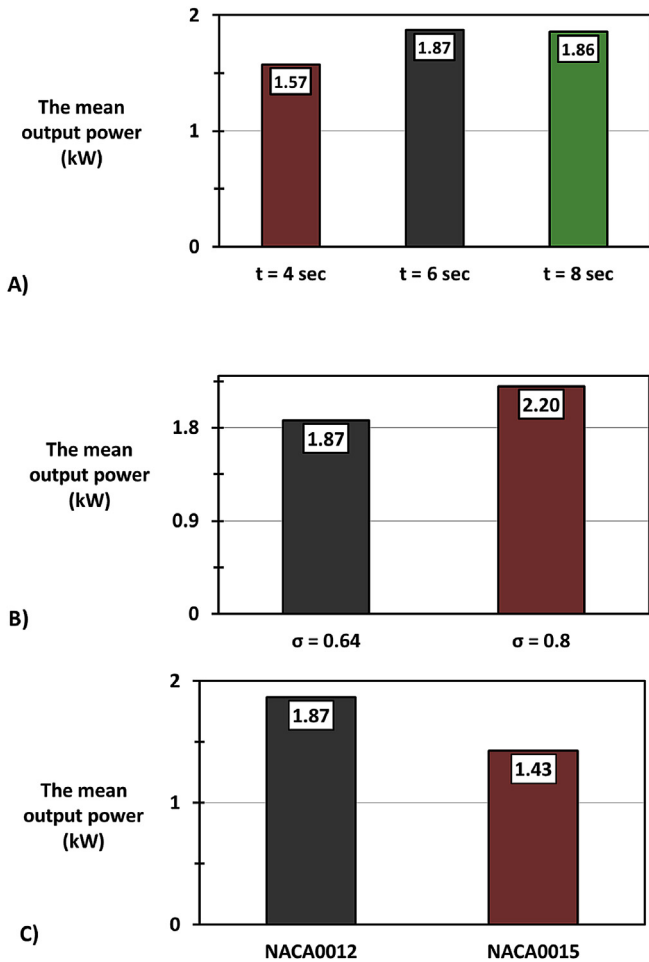
Acknowledgements

References

[1] Rosa AVd. Fundamentals of renewable energy processes. third ed. United States of America: Elsevier Academic Press; 2012.

[2] Falcão AFdO. Wave energy utilization: a review of the technologies. Renew Sustain Energy Rev 2010;14:899—918.

[3] Twidell J, Weir T. Renewable energy resources. second ed. New York, USA: Taylor & Francis; 2006.

[4] Shehata AS, Xiao Q, Saqr KM, Alexander D. Wells turbine for wave energy conversion: a review. Int J Energy Res 2016. http://dx.doi.org/10.1002/er.3583.

[5] Whittaker FAMTJT. Design optimisation of axisymmetric tail tube buoys. In: IUTAM, symposium on hydrodynamics of ocean wave energy conversion, Lisbon, July; 1985.

[6] Whittaker TJJ, McIlwain ST, Raghunathan S. Islay shore line wave power station. In: Proceedings European wave energy symposium, paper G6, Edinburgh; 1993.

[7] Raghunathan S. Theory and performance of wells turbine. Queen's University of Belfast; 1980. Rept. WE/80/13R.

[8] Raghunathan S. The wells air turbine for wave energy conversion. Prog Aerosp Sci 1995;31:335—86.

[9] Ghisu T, Puddu P, Cambuli F. Numerical analysis of a wells turbine at different non-dimensional piston frequencies. J Therm Sci 2015;24:535—43.

[10] Curran R, Folley M. Air turbine design for OWCs. In: Cruz IJ, editor. Ocean wave energy. Berlin: Springer; 2008. p. 189—219.

[11] Falcão AFO, Gato LMC. Air turbines. In: Sayigh AA, editor. Comprehensive renewable energy ocean energy. Elsevier, Oxford; 2012. p. 111—49.

[12] Starzmann R. Aero-acoustic analysis of wells turbines for ocean wave energy conversion. Germany: Universitat Siegen; 2012.

[13] Setoguchi T, Takao M. Current status of self rectifying air turbines for wave energy conversion. Energy Convers Manag 2006;47:2382—96.

[14] Raghunathan S, Beattie WC. Aerodynamic performance of contra-rotating Wells turbine for wave energy conversion. ARCHIVE Proc Inst Mech Eng Part A J Power Energy 1996:431—47. 1990—1996 (vol. 204—210), 210.

[15] Curran R, Whittaker TJT, Raghunathan S, Beattie WC. Performance prediction of contrarotating wells turbines for wave energy converter design. J Energy Eng 1998;124:35—53.

[16] Gato LMC, Curran R. The energy conversion performance of several types of wells turbine designs. Proc Inst Mech Eng Part A J Power Energy 1997;211: 133—45.

[17] Mamun M, Kinoue Y, Setoguchi T, Kaneko K, Islam AKMS. Improvement af the performance of the wells turbine by using a very thin elongated endplate at the blade tip. In: The 3rd BSME-ASME international conference on thermal Engineering. Dhaka, Bangladesh: ASME; 2006.

[18] Takao M, Setoguchi T, Kinoue Y, Kaneko K. Wells turbine with end plates for wave energy conversion. Ocean Eng 2007;34:1790—5.

[19] Kim TH, Setoguchi T, Kaneko K, Raghunathan S. Numerical investigation on the effect of blade sweep on the performance of Wells turbine. Renew Energy 2002;25:235—48.

[20] Setoguchi T, Takao M, Itakura K, Mohammad M, Kaneko K, Thakker A. Effect of rotor geometry on the performance of wells turbine. In: The thirteenth international offshore and polar engineering conference. Honolulu, Hawaii, USA: The International Society of Offshore and Polar Engineers; 2003. p. 374—81.

[21] Inoue M, Kaneko K, Setoguchi T, Hamakawa H. Air turbine with self-pitch-controlled blades for wave power generator (Estimation of performances by model testing). JSME Int J Ser II 1989;32:19—24.

[22] Salter S. Variable pitch air turbines. In: Symposium of European wave energy, Edinburgh; 1993. p. 435—42. Proc Euro Wave Energy Symp, Edinburgh.

[23] Sarmento Ajna GL, AfdeO FalcZo. Wave-energy absorption by an OWC device with blade-pitch-controlled air-turbine. In: Proc 6th int offshore mechanics and arctic eng symp, vol. 2. ASME; 1987. p. 465—73.

[24] Setoguchi T, Raghunathan S, Takao M, Kaneko K. Air-turbine with self-pitch-controlled blades for wave energy conversion (estimation of performances in periodically oscillating flow). Int J Rotating Mach 1997;3:233—8.

[25] Takao M, Setoguchi T, Kaneko K, Inoue M. Air turbine with self-pitch-controlled blades for wave energy conversion. Int J Ofihore Polar Eng ISOPE 1997;7:308—12.

[26] Takao M, Setoguchi T, Santhaknmar S, Kaneko K. A comparative study of turbines using pitch-controlled blades for wave energy conversion. In: Proc 2nd int symp fluid mechanics and heat transfer, Dhaka; 1997. p. 243—50.

[27] Vakalis SA. Real-time control of OWC with a variable pitch-angle turbine. In: Proceedings of the fourth European wave energy conference, Denmark; 2000. p. 309—18.

[28] Thakker FP, Bajeet ES. CA9: analysis of a stall-resistant aerofoil in view of wave power conversion. In: Proceedings of the 11th International offshore and polar Engineering conference, Stavanger, Norway; 2001. p. 614—23.

[29] Mohamed MH, Janiga G, Pap E, Thévenin D. Multi-objective optimization of the airfoil shape of wells turbine used for wave energy conversion. Energy 2011;36:438—46.

[30] Shaaban S. Insight analysis of biplane wells turbine performance. Energy Convers Manag 2012;59:50—7.

[31] Shehata AS, Saqr KM, Shehadeh M, Xiao Q, Day AH. Entropy generation due to viscous dissipation around a wells turbine blade: a preliminary numerical study. Energy Procedia 2014;50:808—16.

[32] Shehata AS, Saqr KM, Xiao Q, Shehadeh MF, Day A. Performance analysis of wells turbine blades using the entropy generation minimization method. Renew Energy 2016;86:1123—33.

[33] Soltanmohamadi R, Lakzian E. Improved design of Wells turbine for wave energy conversion using entropy generation. Netherlands: Meccanica, Springer; 2015. p. 1—10.

[34] Pope K, Dincer I, Naterer GF. Energy and exergy efficiency comparison of horizontal and vertical Axis wind turbines. Renew Energy 2010;35:2102—13.

[35] Baskut O, Ozgener O, Ozgener L. Effects of meteorological variables on exergetic efficiency of wind turbine power plants. Renew Sustain Energy Rev 2010;14:3237—41.

[36] Redha AM, Dincer I, Gadalla M. Thermodynamic performance assessment of wind energy systems: an application. Energy 2011;36:4002—10.

[37] Ozgener O, Ozgener L. Exergy and reliability analysis of wind turbine systems: a case study. Renew Sustain Energy Rev 2007;11:1811—26.

[38] Baskut O, Ozgener O, Ozgener L. Second law analysis of wind turbine power plants: Cesme, Izmir example. Energy 2011;36:2535—42.

[39] Mortazavi SM, Soltani MR, Motieyan H. A Pareto optimal multi-objective optimization for a horizontal axis wind turbine blade airfoil sections utilizing exergy analysis and neural networks. J Wind Eng Ind Aerodyn 2015;136: 62—72.

[40] Şöhret Y, Açıkkalp E, Hepbasli A, Karakoc TH. Advanced exergy analysis of an aircraft gas turbine engine: splitting exergy destructions into parts. Energy

2015;90:1219–28.

[41] Ghazikhani M, Khazaee I, Abdekhodaie E. Exergy analysis of gas turbine with air bottoming cycle. Energy 2014;72:599–607.

[42] Sue D-C, Chuang C-C. Engineering design and exergy analyses for combustion gas turbine based power generation system. Energy 2004;29:1183–205.

[43] Alklaibi AM, Khan MN, Khan WA. Thermodynamic analysis of gas turbine with air bottoming cycle. Energy 2016;107:603–11.

[44] Yucer CT. Thermodynamic analysis of the part load performance for a small scale gas turbine jet engine by using exergy analysis method. Energy 2016;111:251–9.

[45] Mohamed MH, Shaaban S. Numerical optimization of axial turbine with self-pitch-controlled blades used for wave energy conversion. Int J Energy Res 2014;38:592–601.

[46] Mohamed MH, Shaaban S. Optimization of blade pitch angle of an axial turbine used for wave energy conversion. Energy 2013;56:229–39.

[47] Mørk G, Barstow S, Kabuth A, Pontes MT. Assessing the global wave energy potential. In: 29th international conference on ocean, offshore mechanics and arctic Engineering. Shanghai, China: ASME; 2010.

[48] Barstow S, Mørk G, Lønseth L, Mathisen JP. World waves wave energy resource assessments from the deep ocean to the coast. In: The 8th European wave and tidal energy conference, proceedings of the 8th European wave and tidal energy conference, Uppsala, Sweden; 2009.

[49] Zodiatis G, Galanis G, Nikolaidis A, Kalogeri C, Hayes D, Georgiou GC, et al. Wave energy potential in the Eastern Mediterranean Levantine Basin. An integrated 10-year study. Renew Energy 2014;69:311–23.

[50] Ayat B. Wave power atlas of Eastern Mediterranean and Aegean Seas. Energy 2013;54:251–62.

[51] Sheldahl RE, Klimas PC. Aerodynamic characteristics of seven symmetrical airfoil sections through 180-Degree angle of attack for use in aerodynamic analysis of vertical Axis wind turbines. In: Sandia National Laboratories energy report, the United States of America; 1981. p. 118.

[52] Thorpe TW. An assessment of the art OSPREY wave energy device, ETSU-R-90, Dti. 1995.

[53] Mamun M. The study on the hysteretic characteristics of the wells turbine in a deep stall condition. Japan: Energy and Material Science Graduate School of Science and Engineering, Saga University; 2006. p. 141.

[54] Dahlstrom S. Large eddy simulation of the flow around a high-lift airfoil. Goteborg, Sweden: Department of Thermo and Fluid Dynamics, Chalmers University of Technology; 2003. p. 62.

[55] Hinze JO. Turbulence. New York: McGraw-Hill Publishing Co.; 1975.

[56] Launder BE, Spalding DB. Lectures in mathematical models of turbulence. London, England: Academic Press; 1972.

[57] Hirsch C. Numerical computation of internal and external flows: the fundamentals of computational fluid dynamics. Elsevier Science; 2007.

[58] Bejan A. Entropy generation minimization- the new thermodynamics of finite-size devices and finite-time processes. Appl Phys Rev 1996;79: 1191–218.

[59] Iandoli CL. 3-D numerical calculation of the local entropy generation rates in a radial compressor stage. Int J Thermodyn 2005;8:83–94.

[60] De Moura CAK, Carlos S. The Courant–Friedrichs–Lewy (CFL) condition: 80 years after its discovery. 1 ed. Boston: Birkhäuser Basel; 2013.

[61] Thakker A, Abdulhadi R. Effect of blade profile on the performance of wells turbine under unidirectional sinusoidal and real sea flow conditions. Int J Rotating Mach 2007;2007:1–9.

[62] Thakker A, Abdulhadi R. The performance of wells turbine under bi-directional airflow. Renew Energy 2008;33:2467–74.

[63] Torresi M, Camporeale SM, Pascazio G. Detailed CFD analysis of the steady flow in a wells turbine under incipient and deep stall conditions. J Fluids Eng 2009;131:071103.

[64] Torresi M, Camporeale S, Pascazio G. Performance of a small prototype of a high solidity wells turbine. In: Seventh European conference on turbomachinery fluid dynamics and thermodynamics, Athens, Greece; 2007.

[65] Torresi M, Camporeale S, Pascazio G. Experimental and numerical investigation on the performance of a wells turbine prototype. In: Seventh European wave and tidal energy conference, Porto, Portugal; 2007.

[66] Raghunathan S, Curran R, A.W.T.J. T.. Performance of the Islay Wells air turbine. Inst Mech Eng Part A J Power Energy 1995;209:55–62.

[67] Boake CB, Whittaker TJT, Folley M, Ellen H. Overview and initial operational experience of the LIMPET wave energy plant. In: The twelfth International offshore and polar Engineering conference. Kitakyushu, Japan: The International Society of Offshore and Polar Engineers; 2002. p. 586–94.

[68] Whittaker TJTM, S.J., Raghunathan S. A review of the Islay shoreline wave power station. In: Proceedings of European wave energy symposium, Edinburgh, Scotland; 1993. p. 283–6.

[69] Heath T. Islay LIMPET project monitoring, ETSU V/06/00180/00/Rep, Dti Pup URN No 02/1435. 2002.

[70] Wavegen. Research into the further development of the LIMPET shoreline wave energy plant, Dti, V/06/00183/00/Rep. 2002.

[71] Heath T, Whittaker TJT, Boake CB. The design, construction and operation of the LIMPET wave energy converter. In: O.I.a.I. S., editor. The 4th European wave energy conference. Aalborg, Denmark: Danish Technological Institute, Denmark; 2000. p. 49–55.

[72] Belfast TQsUo. Islay LIMPET wave power plant, non-nuclear energy programme Joule III, CORDIS, JOR3-CT98-0312. 2002.

[73] Tv H. The development of a turbo-generation system for application in OWC breakwaters. In: Afo F, editor. Proceedings of the 7th European wave tidal energy conference, Porto, Portugal; 2007.

[74] Torre-Enciso Y, Ortubia I, Aguileta LILd, Marqués J. Mutriku wave power plant: from the thinking out to the reality. In: Proceedings of the 8th European wave and tidal energy conference, Uppsala, Sweden; 2009. p. 319–29.

[75] Washio Y, Osawa H, Nagata FFY, Furuyama TFH. The offshore floating type wave power device 'Mighty Whale': open sea tests. In: C. JS, editor. Proceedings of the 10th International offshore polar Engineering conference, Mountain View, CA, USA. Seattle, WA, USA; 2000. p. 373–80.

[76] Falcao AFdS, Whittaker TJT, Lewis AW. Design of a shoreline wave power plant for the island of Pico, Azores. In: Proceedings of the 2nd European wave power conference; 1995.

[77] Falcao AFd. The shoreline OWC wave power plant at the Azores. In: Proceedings of 4th European wave energy conference, Denmark; 2000. p. 42–7.

[78] Falcao AFdOJ, P.A.P.. OWC wave energy devices with air flow control. Ocean Eng 1999;26:1275–95.

[79] Falcao AFd. Control of an oscillating-water-column wave power plant for maximum energy production. Appl Ocean Res 2003;24:73–82.

[80] Falcao AFd. Stochastic Modelling in wave power-equipment optimisation: maximum energy production versus maximum profit. Ocean Eng 2004;31: 1407–21.

[81] Falcao AFd. Control of an oscillating-water-column wave power plant for maximum energy production. Appl Ocean Res 2002;24:73–82.